Impact of electrode porosity architecture on electrochemical performances of 1 mm-thick LiFePO4 binder-free Li-ion electrodes fabricated by Spark Plasma Sintering

Rakesh Elango, Arina Nadeina, François Cadiou, Vincent de Andrade, Arnaud Demortière, Mathieu Morcrette, Vincent Seznec

Impact of Electrode Porosity Architecture on Electrochemical Performances of 1mm-thick $LiFePO_4$ Binder-free Li-ion Electrodes Fabricated by Park Plasma Sintering

Rakesh Elango,[ab] Arina Nadeina,[ab] François Cadiou,[ab] Vincent De Andrade,[d] Arnaud Demortière,[abc] Mathieu Morcrette,[abc] and Vincent Seznec[abc1]

a. *Laboratoire de Réactivité et de Chimie des Solides, Université de Picardie Jules Verne, CNRS UMR7314, 15 Rue Baudelocque, 80039 Amiens, France.*

b. *RS2E, Réseau Français sur le Stockage Electrochimique de l'Energie, FR CNRS 3459, France.*

c. *ALISTORE-ERI, 80039, FR CNRS 3104, France.*

d. *Advanced Photon Sources, Bldg. 401/Rm A4115, Argonne National Laboratory 9700 S. Cass Ave. Argonne, IL 60439, USA.*

Abstract:

Thick electrodes with high active material loadings have been intensively studied over the last couple of decades in pursuit of achieving high energy density systems. To optimize and enhance the electrochemical performance of such electrodes, one has to control the pore morphology by, for example, varying the pore size and shape, and the level of porosity. In the present work, the fabrication of thick binder-free $LiFePO_4$ (LFP) electrodes with two different pore sizes (12 and 20 μm) and porosities (21 vol.% and 44 vol.%) using Spark Plasma Sintering (SPS) and templating approach is reported. The well-controlled porous architecture inside the thick electrodes is realized by fine-tuning experimental parameters. The impact of porosity architecture on electrochemical performance is quantified and correlated with the 3D tortuosity values determined from both micro-computed tomography and electrochemical impedance-based experimental methods. Based on the micro-computed tomography data analysis, estimated tortuosity values along X, Y, and Z axes reveal an

[1] *Corresponding author:* **Vincent SEZNEC**, **e-mail**: vincent.seznec@u-picardie.fr, **tel**.: 03 22 82 53 31, **address** : Laboratoire de Réactivité et Chimie des Solides - UMR CNRS 7314, Université de Picardie Jules Verne, HUB de l'énergie, 15 rue Baudelocque - 80000 Amiens, France

anisotropic effect perpendicularly to the SPS compression axis (Z-direction). This is particularly profoundly observed in the samples with larger pores (20 μm). The correlation between morphological properties and the rate capability performance is established indicating that the capacity loss happens mainly due to the Li-ion diffusion limitations.

Keywords: thick electrodes, cathode material, Spark Plasma Sintering, μ-CT, tunable porous architecture

1. Introduction

Lithium-ion batteries (LIB) have been dominating the portable electronics and hybrid/all-electric vehicle markets due to the vast improvements in their energy and power densities while maintaining an excellent cycle life [1]. Overall Li-ion battery performance depends on different factors, such as choice of active materials, cell/pack designs, operating temperatures, type of charging modes, and electrode architectures [2–7]. The latter is greatly impacted by the pore design (size, shape, and orientation), tortuosity values, and a type of porosity (dead-end, open, and closed). Indeed, in the Newman's continuous model for porous electrodes, the intrinsic and effective ionic and electronic conductivities are directly proportional to the ratio between porosity and tortuosity values, which, in turn, play a dramatic role in various electrochemical systems, such as batteries, supercapacitors, and fuel cells [8–12]. To properly design the electrode's architecture, a large variety of synthesis and electrode preparation techniques have been developed [13–15]. Templating approach is one of the methods used to design electrodes with well-interconnected and controlled pore architectures. This method is based on the introduction of a soft or hard templating agent during the electrode preparation step followed by a template removal step. The final pore size and shape can varied by adjusting the initial size of the templating agent.

In the conventional Li-ion batteries, electrodes are prepared by coating the current collector (typical thickness: 12-20 μm) with the liquid slurry composed of active material, binder, and conducting additives (typically with weight ratios of 94%, 3%, 3%, respectively). The coated electrode is then dried by solvent evaporation and calendered with high uniaxial pressure of around 1 ton per linear inch to promote better adhesion between the active material and the current collector and to achieve the desired thickness (typically between 50 and 100 μm) and porosity of the final electrode (around 30%). Unfortunately, the calendering step induces an increase in tortuosity along the Li-ion transport direction [16].

In the search of reducing the tortuosity values, various alternative fabrication strategies, such as co-extrusion with sintering [17], magnetic templating [18], and freeze casting[19] have been proposed to fabricate $LiCoO_2$, $LiNi_{0.8}Co_{0.15}Al_{0.05}O_2$, and graphite electrodes. These strategies seem to greatly improve the transport kinetics of lithium ions at high C-rates leading to three times better performance compared to the conventional tape-casted electrodes. However, the quantification of their tortuosity parameters remains rather difficult. Several studies showed improved tortuosity measurements of battery electrodes and separators using electrical impedance spectroscopy (EIS), nuclear magnetic resonance (NMR), and X-ray synchrotron experiments [20–23]. Tortuosity value greatly depends on the electrode's pore morphology, such as pore volume fraction, pore size/shape, and on the distribution of particle arrangement inside the electrodes. The influence of altering these parameters on the change in tortuosity was studied by measuring the ionic resistances of lithium ions through the pores inside the thick electrodes [20,21].

To increase the energy density of the electrodes ($Wh.kg^{-1}$), one either has to increase the electrode thickness (thus increasing the amount of active material) or to reduce the number of inactive components, such as the current collector, separator, packaging, and binder. High active material loading could be achieved by using different fabrication methods, such as sintering, replacement of current collector films by electrode-incorporated current collector foam, preparation of textile-based

electrodes [13,17,24]. Among others, Spark Plasma Sintering stands out as a promising technique to make thick electrodes with strong grain-to-grain bonding and stable interfaces [25, 26].

Recently, the results for 1mm thick binder-free $LiFePO_4$ and $Li_4Ti_5O_{12}$ electrodes using the combined strategy of the Spark Plasma Sintering technique and templating approach have been reported by R. Elango *et al* [27]. This study can be seen as proof of concept and demonstrates the achievement of 4-5 times higher areal capacity of the thick electrodes when compared to the conventional electrodes [28].

In the present work, we continue the investigation of 1mm thick binder-free LFP electrodes and study the correlation between the electrode architecture and its electrochemical performance. Herein, the electrodes were fabricated with two different pore sizes and two porosity values. Rate capability tests of the thick LFP electrodes in half-cell arrangements (vs. Li/Li^+) were carried out to identify the best pore architecture for optimized electrochemical performance. Measurements of electrodes tortuosities using electrical impedance spectroscopy were performed. The 3D visualization and the microstructural characteristics of the thick electrodes were obtained using micro-computed tomography technique and image processing.

2. Experimental part

Synthesis of NaCl crystals

NaCl crystals with two different particle sizes were prepared.

2 ± 0.6 μm particles were synthesized by precipitation using acetyl chloride and sodium acetate trihydrate as precursors [29]. 2 g of sodium acetate trihydrate (Sigma-Aldrich, ≥ 99.0%) were dissolved in 10 ml of ethanol and then 20 ml of acetyl chloride (Sigma-Aldrich, ≥ 99.0%) were added drop-wise to the solution under stirring. Acetyl chloride acts as a strong donor of chlorine which reacts with sodium acetate to form sodium chloride crystals. The reaction is slightly exothermic; therefore 100 ml of absolute ethanol (Sigma-Aldrich, 99.9%) was added to cool down the mixture. Obtained white

precipitate was washed by centrifugation in absolute ethanol at 6000 rpm, 5min three times, and dried in the oven at 70°C overnight.

13.2 ± 3.7 μm particles were prepared by simply grinding the commercial salt (Sigma-Aldrich, ≥ 99.5%) in a mortar for 20 min.

Scanning Electron Microscopy images of the prepared NaCl crystals were obtained (Fig. 3.1 a-b) and Fig. SI1). The size particle distributions were determined using FIJI® software [30].

SPS experiments

Pellets of two different porosities (theory: 20 vol.% and 40 vol.%) with two different pore sizes (12 μm (μm) and 20 μm; the initial size of NaCl templates: 2 μm and 13.2 μm, respectively) each were prepared by mixing the respective amounts of carbon-coated $LiFePO_4$ (1.77 wt.% coating, Targray, battery grade) as-prepared NaCl, and carbon black (Timcal, battery grade) (volume ratios of LFP/NaCl/C-45 are 70/20/10 and 50/40/10 (or 80/14/6 and 62.7/30.8/6.5 in weight ratios) for 20% and 40% porous electrodes, respectively; the mass goal of the final composite is 450 mg) in a mortar for 30 min, then placing the powder in the 10 mm diameter graphite dies preliminary lined with graphite paper. Cold-pressing of the mixture was then performed in a hydraulic press for 5 min under 2 tons followed by sintering in the FCT GmbH HPD10 machine according to the protocol: 1) evacuation of the SPS chamber down to 10^{-3} Pa; 2) heating up to 650°C and pressing up to 125 MPa for 5 min with 100°C min^{-1} rate; 3) cooling down to 25°C with a natural rate of the SPS machine (ca. 200°C min^{-1}) while keeping the pressure at 125MPa; 4) releasing the pressure. Temperature control during the SPS procedure was performed by the thermocouple placed in the middle of the die.

The compactness of the LFP-NaCl-C pellets was determined to be 94% irrespective of the particle size and the amount of NaCl crystals used in composite preparation.

After sintering, the pellets were recovered from the die and polished using the sandpaper down to 1 mm thickness. Subsequently, the pellets were washed using a vacuum-assisted impregnation method using distilled water to leach out the NaCl template. The complete dissolution of all NaCl was confirmed by the weight loss calculation, using X-ray diffraction, and Energy-dispersive X-ray spectroscopy (EDX). Scanning Electron Microscopy images of the initial $LiFePO_4$ crystals as well as carbon black particles were obtained and are depicted in Figure SI 1.2 in Supporting Information.

Electrochemical measurements

Swagelok cells were assembled in an Ar-filled glovebox with a moisture level below 1 ppm. Li foil was used as a half-cell counter electrode, glass fiber (Whatman GF/A) was used as a separator, commercial LP30 (1M solution of $LiPF_6$ salt in 1:1 wt.% EC/DMC) was used as a liquid electrolyte. 1mm-thick LFP electrode was cut by a diamond saw in the middle resulting in a piece of 10 mm x 1 mm x 1 mm with a surface area of 0.1 cm^2. Cells were galvanostatically cycled using a Biologic VMP-3 (Biologic SAS, France) instrument at C-rates of C/20 and C/5. The electrochemical measurements were carried out at room temperature.

EIS

Electrical impedance spectroscopy using symmetrical cell setup for the measurement of ionic resistance through the pores of 1-mm thick LFP electrodes was performed. One pair of 1-mm thick LFP electrodes with similar microstructural features (porosity and pore size) was used for the impedance measurements. In this experiment, n-tetra butyl ammonium perchlorate (n-$TBAClO_4$) salt was dissolved in ethylene carbonate and di-methylene carbonate in a weight ratio of 1:1 (EC: DMC). Such electrolyte was purposefully chosen to avoid lithium intercalation/de-intercalation across the solid/liquid interface of the LFP electrodes. The intrinsic ionic conductivity of the as-prepared electrolyte was measured using a conductivity cell and was found to be 0.062 mS cm^{-1} at 20°C, which correlates well with the literature [20].

A frequency range of 200 kHz to 0.5 mHz was applied with an amplitude signal of 10 mV. The symmetrical LFP electrodes were assembled in the glovebox and tested at a constant temperature of 25°C. The measured ionic impedance (R_{ion}) of the cell was obtained by the sum of impedances of the individual electrodes and hence factor two is written in the equation 1.7 where A is geometric surface area (cm^2), κ is the bulk conductivity of the used electrolyte (S cm^{-1}), ε is electrode porosity (%), and d is electrode thickness (cm).

Tomography measurements

In the present work, μ-CT tomography measurements of thick binder-free LFP electrodes were carried out at the synchrotron source at Advanced Photon Source (APS) in Argonne National Laboratory (ANL, USA) at the beamline 32ID with the Full Field Transmission X-ray Microscopy setup. The 1mm thick electrode was characterized with nearly 1200 images generated at an angular step of 0.15°. In the μ-CT mode, the field of view is 1mm with a spatial resolution of 1.3 μm. The tomography data set acquired as a function of the rotation angle is reconstructed into an XYZ dataset using a back-projection method based on Radon transform. The tomogram reconstruction was done using the APS python library in Tomopy. The segmentation procedure as well as the geometric tortuosity determination was done using FIJI® software. The TXM and binary images after the thresholding step of two LFP electrodes in the Z-direction are depicted in Supporting Information Fig. SI3. The 3D reconstructed images of LFP electrodes were illustrated by AMIRA software (Fig.3) [31]. The 3D visualizations of the local tortuosity values were generated using ParaView® software [32].

3. Results and Discussion

3.1 Electrodes preparation and SEM analysis

Figure 1 schematically represents thick electrode fabrication using SPS and templating approach. The digital pictures and SEM images of the full 1 mm thick electrodes are shown in Figure 1 (c-f). The difference in the pore sizes of two samples prepared with different NaCl crystals (with average

crystallite sizes of 2 μm and 13 μm) is seen on the cross-sectional images of the electrodes (Fig.1 g-j). The average pore sizes of the electrodes were found to be 12 ± 2 μm and 20 ± 8 μm for 2 μm and 13.2 μm initial templating agent particle sizes, respectively (cf. Supporting Information, Fig. SI1). The increase in pore sizes, as compared to the initial size of NaCl particles, results from the manual mixing (here: grinding) of the initial composite as well as from the SPS process during which the salt particles might undergo a slight agglomeration. Fig.1 j) shows a clear elongation of pores perpendicular to the Z-direction caused primarily by the uniaxial pressure along the Z-axis during the SPS procedure. This pore anisotropy is particularly clearly observed in the case of 20 μm pore-sized electrodes (initial salt particles size: 13 μm) and seems to be greatly minimized for the smaller pore-sized electrodes due to the higher uniformity and narrower size distribution of the used template particles (Fig. 1 g) and h). Thereby, in the latest case, one can expect to have better pore interconnectivity which could lead to the enhanced diffusion rate of Li-ions in the liquid phase.

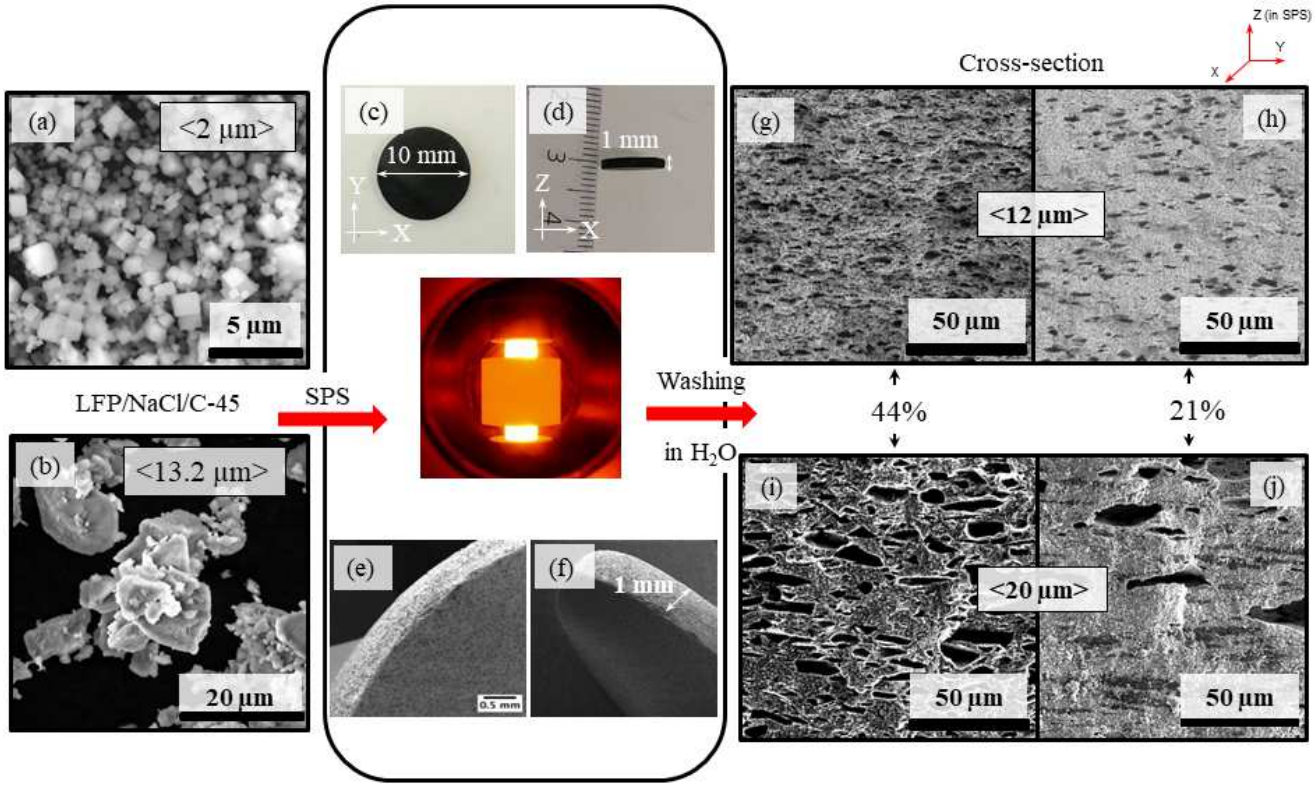

Figure 1. Thick $LiFePO_4$ electrode fabrication scheme with two different pore sizes: a-b) NaCl particles: 2 μm and 13 μm; c-f) Digital pictures and SEM images of LFP thick electrode; g-j) a

cross-sectional view of thick LFP electrodes with 44% and 21% porosity: g-h) 12 μm pore size; i-j) 20 μm pore size.

However, SEM images provide only 2D morphological information; the average pore size and other microstructural properties such as porosity, pore size distribution, and specific surface area were determined more precisely using tomography measurements.

3.2 Electrochemical performance

Charge-discharge cycling curves at C/20 and C/5 of four LFP half-cells (two different pore sizes with two porosity values each) are shown in Figure 2 a) and b).

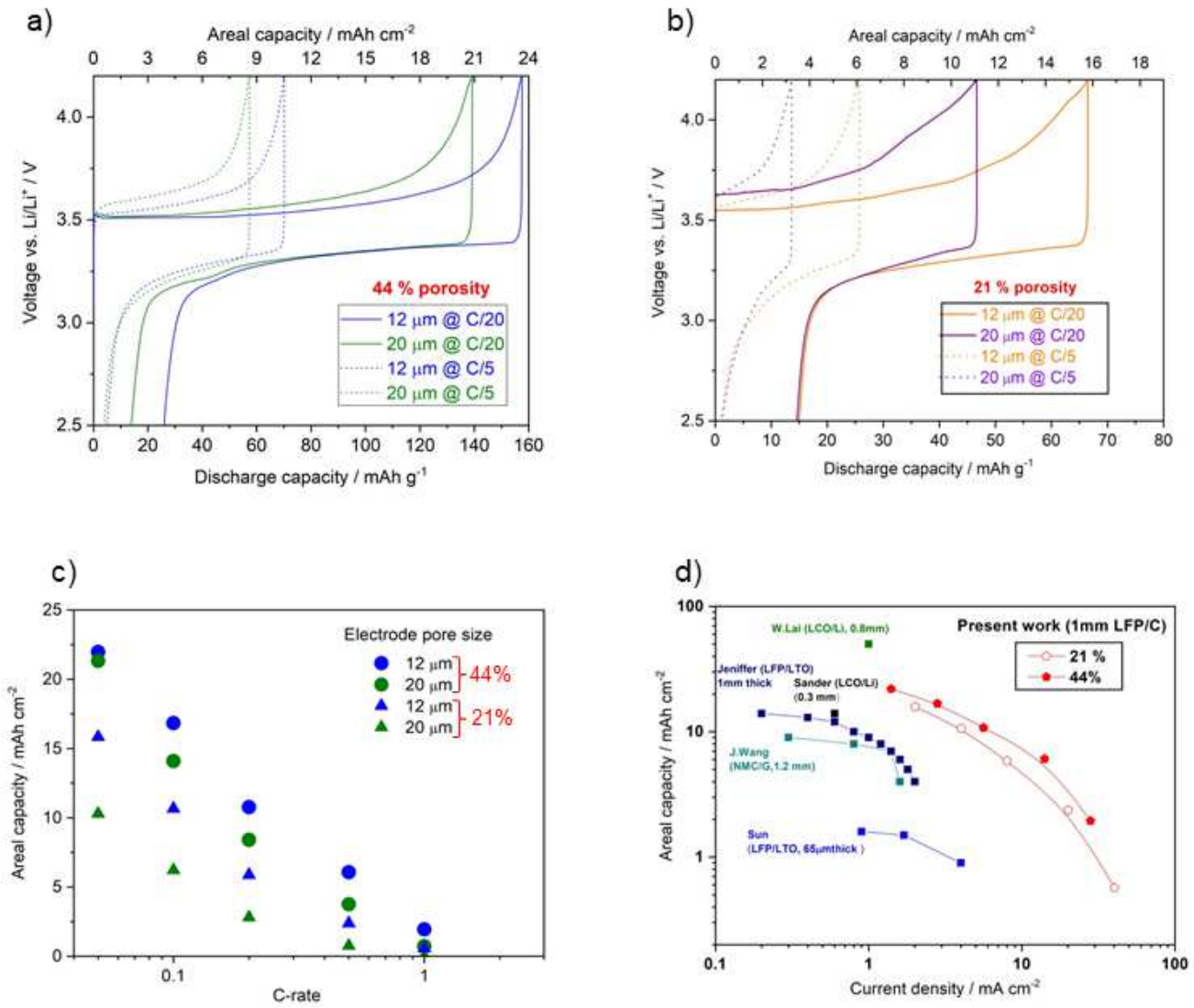

Figure 2. Charge-discharge profiles of 1-mm thick LFP-C electrodes with 12 μm and 20 μm pore sizes against lithium at C/20 and C/5 rates: a) 44% porosity, b) 21% porosity; c) Ragone plot showing the areal capacities vs. C-rate for four different LFP half-cells as a function of pore size and porosity; d) Areal capacity vs. current density values of 1 mm thick LFP electrodes (44% and 21% porosity with 12 µm pore size each) compared to the literature [13,17,18,24,33]

Firstly, the effect of porosity on the electrochemical performance was analyzed. It was found that the 44% porous electrode with a pore size of 12 μm delivers more than 2 times as much gravimetric capacity on the first charge at C/20 as the 21% porous sample (157.6 mAh g^{-1} vs. 66.5 mAh g^{-1}, respectively). The same tendency is observed for both samples at a higher C-rate (C/5). This behavior is

to be expected, since, as mentioned beforehand, the 44% porous electrode should have better pore connectivity which promotes electrolyte impregnation resulting in higher active material accessibility. Besides, lower achieved capacity values of 21% porous electrodes could also result from incomplete leaching of the templating agent which, in turn, contributes to the 'dead mass' of the electrode and inhibits full active material utilization.

Secondly, the effect of the pore size within the same-porosity electrodes was studied. For both 44% and 21% porous electrodes, the 12 μm pore-sized samples showed higher achieved capacity at both C/20 and C/5 cycling rates. This result is clearly in agreement with the lower tortuosity value of 12 μm pore-sized electrodes when compared to 20 μm as determined by the micro-computed tomography and EIS methods shown in the Tortuosity Value Determination section. A similar improved trend was obtained for the co-extruded and sintered LCO electrodes where the minimization of the pore channel spacing played a significant role in the higher-rate electrochemical performance [34].

The difference in the polarization evolution of all four samples follows the same trend and is easily noticeable in Fig. 2 a), b). 44% porous electrodes (both 12 μm and 20 μm pore-sized) possess lower overall polarization than samples with 21% porosity at any employed C-rate as a result of higher electrolyte accessibility to the active material. Within the same-porosity electrode, however, the pore size plays little to no role in the overpotential evolution resulting in nearly the same over polarization at C/20 and C/5 rates for both 44% and 21% porous electrodes.

Figure 2 c) shows the Ragone plot of 21% and 44% porous electrodes depicting the areal capacity as a function of C-rate. It is obvious that at low C-rate the 44% porous electrode performs significantly better than 21% while at elevated C-rates (here: 1C) the difference becomes almost negligible as capacity values for both electrodes drop almost to zero. Such behavior is typical for thick electrodes and is to be anticipated as at higher C-rates the charge-transfer resistance at the solid/liquid interphase as well as the ionic resistance in the pores of the electrode increase significantly. Besides, at higher C-rates the effect of mass transport limitations is observed more profoundly than at low C-rates (here: C/20).

Within the same porous electrode, the effect of the pore size on the electrochemical performance at different C-rates has the same tendency as observed earlier (Fig. 2 a-b): on average, smaller-sized electrodes (i.e. 12 μm) perform better than their larger (20 μm) counterparts. This behavior could be assigned to better pore connectivity and lower pore tortuosity in the case of smaller-sized electrodes as discussed in the next section.

Consequently, the best electrochemistry is obtained for 44% porous 12 μm pore-sized electrode (C/20: 157.6 mAh g^{-1} (23.9 mAh cm^{-2}); C/5: 70.1 mAh g^{-1}(10.1 mAh cm^{-2})). At C/20 current rate, the areal capacity values of the thick 44% porous electrode are 4-5 times higher than those of the conventional film-based electrodes.

The superior performance of the thick SPSed electrodes was compared to the recently reported thick electrodes in the literature (Fig. 2d) [13,17,18,24,33]. Fig. 2d) shows that even at high current densities (C/5), the obtained areal capacities of the samples present in this work are higher than those reported in the literature. These results clearly show that the SPS and templating approach is a very beneficial technique when it comes to the preparation of thick electrodes with controlled pore morphology.

3.3 Tortuosity value determination

3.3.1 Micro-computed tomography analysis: Tau factor and geometrical tortuosity determination

X-ray tomography analysis is a powerful non-destructive tool in the analysis of the structure and morphology of (thick) electrodes. Not only it allows a quite accurate pore network extraction but also helps to determine the electrode's pore volume fraction, pore size distribution, pore network tortuosity, and phase percentage.

Considering the enhanced electrochemical properties of 44% porous electrodes as compared to the 21% porous ones, a deeper study of the pore morphology by tomography analysis and by EIS measurements was performed solely on the 44% porous electrodes as they are of higher practical interest. The 3D rendered images based on the obtained tomography data of the 12 μm and 20 μm pore-sized samples are depicted in Figure 3. Here, yellow color represents the void (pores) while blue and green represent the solid phase of the electrode.

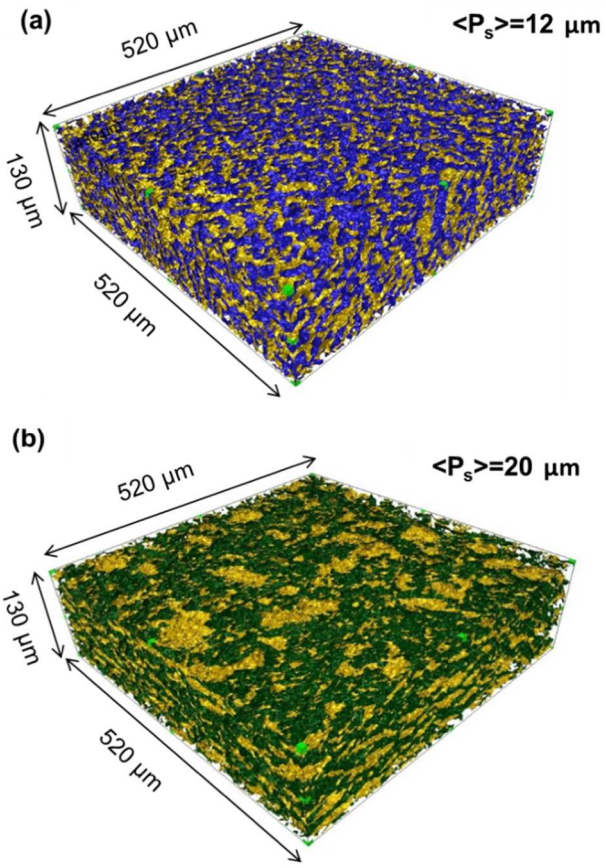

Figure 3. Tomography data-based 3D rendered images of 44% porous LFP thick electrode showing the difference in pore size: a) 12 μm, and b) 20 μm

As can be seen from Figure 3, the 12 μm pore-sized electrode (Fig. 3 a) has more homogeneous pore network connectivity as compared to the 20 μm pore-sized electrode (Fig. 3 b) which shows pore clustering caused by the initial NaCl template particles agglomeration.

Pore tortuosities of thick electrodes were determined in three orthogonal directions using the Tau factor on MATLAB application® developed by Cooper *et al.*, Imperial College of London, UK [35], and geometrical tortuosity calculations using Fiji® software [30]. Tau factor analysis allows carrying out a fast and simple calculation of the tortuosity directly using the microstructural data. The principle of this tool is based on Fick's law of diffusion, which states that the flux (*J*) is directly proportional to the concentration gradient (*dC/dx*). It involves the calculation of the reduction in diffusive transport due to the convoluted electrode geometry of heterogeneous media based on microstructural image data. The solid-state diffusion of lithium-ion is eliminated. In other words, the tortuosity is determined by the ratio of steady-state diffusive flow through a porous volume network to the fully dense control volume of an electrode as shown in equations 1.1-1.3, where F_p and F_{cv} are flux through pore network and control volume, respectively, A_{cv} is a cross-sectional area, L_{cv} is the length, D is the intrinsic diffusivity of the conductive phase, D_{eff} is the effective diffusivity through a porous volume where one phase is conducting and the other phase is insulating, ε is the volume fraction of the conductive phase:

$$F_p = -A_{cv} D_{eff} \left(\frac{\Delta C}{L_{cv}}\right) \tag{1.1}$$

$$F_{cv} = -A_{cv} D \left(\frac{\Delta C}{L_{cv}}\right) \tag{1.2}$$

$$D_{eff} = D \left(\frac{\varepsilon}{\mathcal{T}^2}\right) \tag{1.3}$$

The tortuosity in Z-direction was obtained using Tau factor simulations software. The thresholded image stack was given as an input. The report figure generated by the Tau factor is shown in Supporting Information, Fig. SI2. The three slices (Fig. SI2 a, b, c) represent the binary image of the sample (LFP electrode with 20 μm in the Z-direction) and the corresponding initial and steady-state diffusion simulations performed in a local volume of the electrode. The distribution of concentration and flux in a slice of the volume is illustrated in Fig. SI2 e). Fig. SI2 d) shows a graph of the effective diffusivity

calculated at the top and bottom faces against the iteration number. The convergence of the system was established by analyzing both the rate of change of the top and the base effective diffusivity values. The tortuosity of a shown electrode (44%, 20 μm) in Z-direction was determined to be 2.44 with the phase volume fraction (ε) of 44.4% and effective diffusivity (D_{eff}) of 0.0678 $m^2\ s^{-1}$.

Furthermore, the characteristic tortuosities of both 12 μm and 20 μm pore-sized electrodes of 44 vol. % of porosity were determined. Characteristic tortuosity ($\mathcal{T}_c$) represents an overall contribution of the tortuosities of the electrode in all three directions($\mathcal{T}_x, \mathcal{T}_y, and\ \mathcal{T}_Z$) and could be determined via Eq. 1.4

$$\boldsymbol{\mathcal{T}_C = (3[(\mathcal{T}_X{}^{-1}) + (\mathcal{T}_Y{}^{-1}) + (\mathcal{T}_Z{}^{-1})])^{-1}} \qquad (1.4)$$

As shown in Figure 4 a-b), the definite volume of the LFP electrode (520x520x520 μm) was divided into 8 smaller sub-sections with equal cubic volumes (260x260x260 μm). Each respective sub volume was subjected to the mass diffusive transport simulations using the Tau factor application and the set of localized tortuosity values in three directions was extracted for each subvolume instead of representing a single tortuosity value for the whole electrode (Fig. 4 c-d). For the 12 μm pore-sized 44% porous electrode (Fig. 4 c)), the tortuosity values in three directions are almost the same, while for the 20 μm pore-sized 44% porous electrode one can notice that the tortuosity values in the Z-direction are higher than in X- and Y-directions (Fig.4 d)). Such discrepancy between the tortuosities in the Z-direction and X-, Y-directions in the case of 20 μm pore-sized electrode could originate from anisotropy of the pore shape induced by the sintering procedure under the uniaxial pressure. At the same time, almost no anisotropy in tortuosity values was observed for 12 μm pore-sized electrode as the initial salt template particles showed a narrow pore size and shape distribution leading to almost uniform pore shapes.

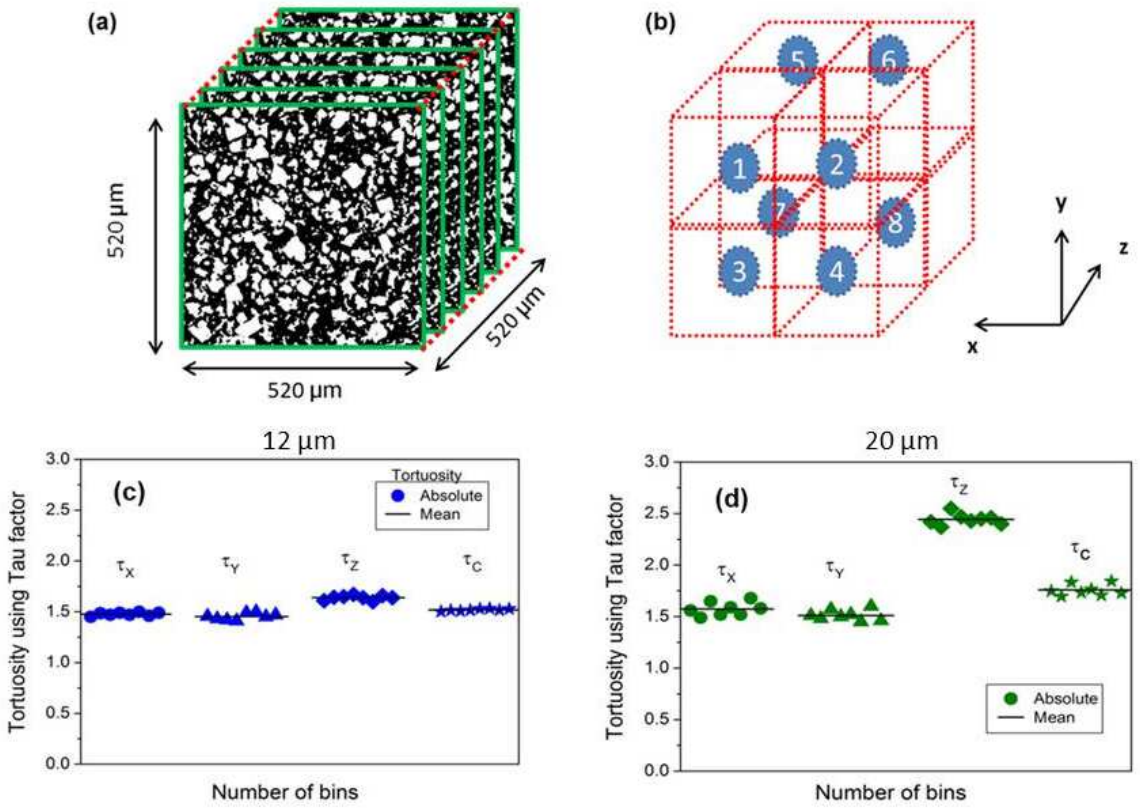

Figure 4. a-b) Tomography analysis of 12 μm and 20 μm pore sized electrode of 44% porosity, c-d) Tortuosity determination using Tau factor for x, y, z directions along with characteristic tortuosity values

Tortuosity calculations were also performed using the geometric definition of tortuosity. For a porous network where L_{pore} is the actual path length through the network and $L_{straight}$ is the direct distance (straight line) between two points or planes, the geometric tortuosity is defined as a ratio between the former and the latter:

$$\tau_{geom} = \frac{L_{pore}}{L_{straight}} \tag{1.5}$$

In the present work, the geometric tortuosity was determined locally using Fiji® software.[30] Firstly, starting from one of the volume sides, a Euclidean distance front was propagated in the porosity phase in a perpendicular direction to the seed plane. Then, another distance front was propagated from the opposite face and the sum of these two distance maps was computed. In the resulting map, each voxel has the value of the shortest path linking the two starting planes and going through the voxel.

Lastly, a local geometric tortuosity map was obtained by dividing the map by the straight distance between the starting planes.

In addition to the tortuosity characterization, Fiji software was also used to determine the pore size distribution using the 'Local thickness' method implemented in Fiji software. This method consists of fitting spheres inside the desired phase to find its maximal local dimension. By this method, the average pore sizes were determined to be 16 μm and 20 μm which correlate well with the pore sizes obtained from the SEM analysis and by the Amira software based on the μ-CT data [31] (12 μm and 20 μm, respectively).

Figure SI4 in Supporting Information represents rendered 3D images of the 16 μm and 20 μm pore-sized microstructures (a) and d), respectively) with 3D visualizations of the most represented local tortuosity values (b-c) and e-f)) generated using ParaView® software [32]. One can notice that the geometric paths remain relatively straight and are gathered in channel-like shapes. Such a configuration of the pore structure is highly beneficial for improving ion diffusion throughout the whole thickness of the electrode. Mean geometric tortuosity values in each direction were calculated and a very similar trend to the one determined with the Tau factor was observed. Here, mean tortuosity values for 12 μm (16 μm) pore-sized sample were found to have a quite isotropic behavior resulting in relatively similar values in all three orthogonal directions while 20 μm pore-sized electrode showed slightly anisotropic behavior yielding increased tortuosity values in the Z-direction. Despite the smaller tortuosity values in the case of geometric calculations due to the method specificity, the overall trend correlates well with the data obtained from the Tau factor analysis. A summary of the tortuosities obtained by different methods along with theory-based calculated values is presented in Table 1.

Table 1. Comparison of $LiFePO_4$ electrode tortuosity values obtained by µ-CT (Tau factor analysis and geometrical tortuosity estimation) and literature-based calculated values

Method	Tortuosity	Average pore size of 44% porous LFP electrode

		12 [μm] (16 μm)	20 [μm]
Tau factor	$\mathcal{T}_X$	1.48	1.59
	$\mathcal{T}_Y$	1.45	1.51
	$\mathcal{T}_Z$	1.64	2.44
	$\mathcal{T}_c$	1.52	1.76
	$\mathcal{O}$	0.12	0.54
	$\mathcal{E}_{total}$	48.0	44.7
Geometric tortuosity	$\mathcal{T}_X$	1.022	1.018
	$\mathcal{T}_Y$	1.012	1.021
	$\mathcal{T}_Z$	1.017	1.037
	$\mathcal{T}_c$	1.017	1.025
Literature	($\mathcal{T}_{Bruggeman}= \mathcal{E}^{0.5}$)	1.44	1.49
	($\mathcal{T}_{Thorat}= 1.8\mathcal{E}^{0.53}$)	2.65	2.75

3.3.2 EIS measurements

Electrical Impedance Spectroscopy is widely used to determine ionic resistance of the electrodes which is mainly quantified by the electrode pore tortuosities. Symmetrical cell approach prevents interference with the counter electrode and/or lithium-ion intercalation.

In the present work, low concentration n-TBAClO_4 (10 mM) was used for the EIS Symmetrical cell measurements to minimize the error in the resistance values especially on the low-frequency intercept obtained in the Nyquist plot. The electronic resistance in the solid phase becomes negligibly small compared to the ionic resistance in the electrolyte phase.

EIS-SC impedance spectra mainly consist of three domains. 1) High-frequency intercept: corresponds to the electrolyte resistance in the separator and other ohmic contacts due to the induction cables and connection wires; no significant differences are observed for two LFP cells with the same porosities but different pore sizes. 2) Middle frequency region: consists of a Warburg line close to 45°

which is more crucial for the determination of ionic resistance through the pores of the electrode. Higher elongation of this line is observed for the 20 μm pore sized electrode corresponding to a higher ionic resistance arising due to the increase in pore length and radii. This region represents the mobility of ions inside the porous electrode, and a large deviation from 45° corresponds to the non-uniform pore shape and size distributions present inside the porous electrode. 3) Low-frequency region: consists of a straight line (in theory: 90°) corresponding to the capacitive behavior of the electrical double layer formed at the electrode-electrolyte interface.

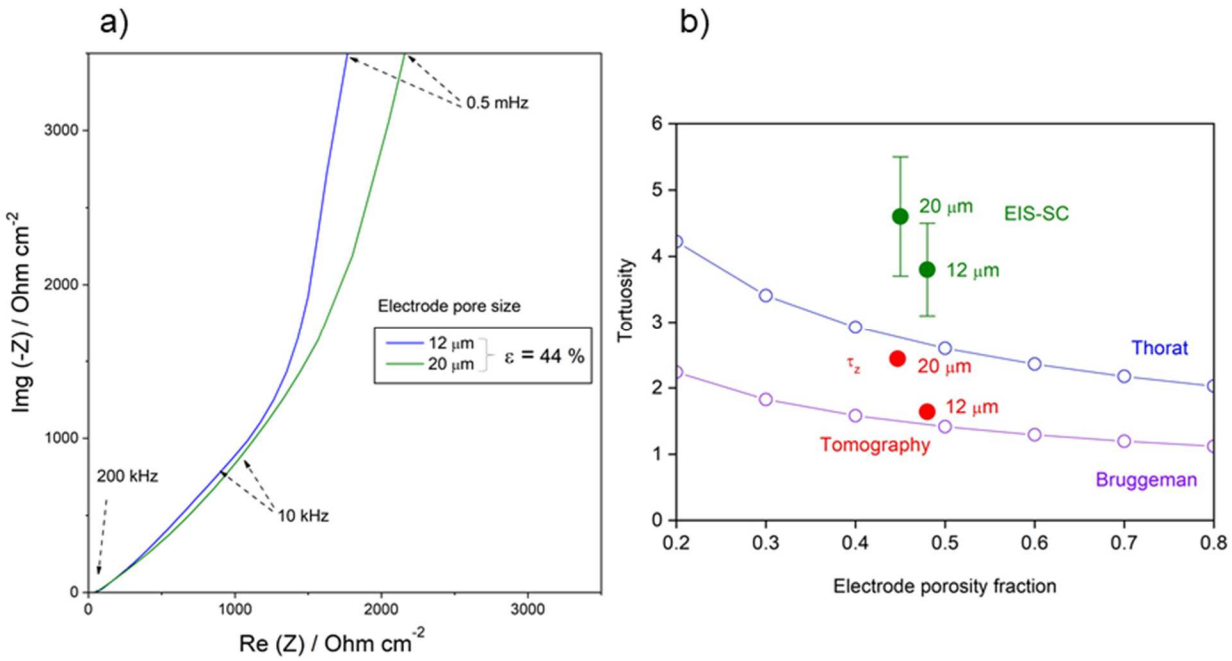

Figure 5. a) EIS-SC spectrum of 12 μm and 20 μm pore sized 44% porous electrode, b) Comparison of thick 44% porous LFP electrode tortuosity values obtained by EIS-SC and tomography methods

The effective ionic resistance of the electrolyte within the electrode porosity (R_{ion}) can be extracted from the impedance data via the following expression [20]:

$$R_{ion} = 3(Re\,|_{Z_{\omega\to 0}} - R_{HFI}) \qquad (1.6)$$

where R_{HFI} is the high frequency (here: 200 kHz) intercept with the real axis Re(Z), $Re\,|_{Z_{\omega\to 0}}$ is the intercept of the extrapolated low-frequency part of the tail (Fig. 5 a) with the real axis Re(Z).

In turn, the tortuosity values could be calculated based on the calculated ionic resistance values (obtained from the impedance spectra) by equation 1.7[20], where A is a geometric surface area of thick LFP electrode, κ is the bulk ionic conductivity of the electrolyte used, ε is the electrode porosity, d is the thickness of the electrode, and R_{ion} is the ionic resistance of the electrode.

$$\tau = \frac{R_{ion}\ A\ \kappa\ \varepsilon}{2d} \tag{1.7}$$

Tortuosity values obtained by this equation for two different pore-sized 44% porous LFP electrodes (12 μm (16 μm) and 20 μm) are 3.8 ± 0.7 and 4.6 ± 0.9, respectively.

EIS-SC experimental results (Figure 5, b) show more than two times higher tortuosity values than the ones obtained by the Tau factor diffusion simulations using micro-tomography data. Since EIS-SC is a macroscopic measurement, it allows determination of the tortuosities of the full pore network including the dead-end pores (pores which are not connected to the main conductive pore network) and closed porosities. On the contrary, the tortuosity values obtained by the tomography analysis are underestimated due to the non-accountability of the dead-end pores which contribute significantly to the transport of lithium ions through the structure. Another limitation of the tomography method is its low spatial resolution (voxel size is 1.3 µm). It is therefore obvious that the pores smaller than 1.3 μm are not taken into account in the calculation, resulting in the smaller tortuosity values. In the future, higher-resolution nano-tomography could be performed to determine the pore tortuosities more accurately.

However, the EIS-SC technique is not totally accurate and contains an intrinsic error. Here, the electronic conductivity of the LFP electrodes is taken as an infinite value which is not the real case, as the electronic conductivity of the carbon-coated LFP particles is still relatively low, leading to large statistical error bars obtained from the repetitive experiments.

4. Conclusions

A comprehensive study of the impact of the electrode architecture on the electrochemical performance of 1mm-thick binder-free LFP/C electrodes was performed showing that the pore morphology strongly influences the electrode electrochemical properties.

It has been observed that on average 44% porous electrode performs better than 21% porous electrode delivering more than 1.5 times more capacity regardless of the C-rate (with 12 μm (16 μm) pore size at C/20: 23.6 mAh cm^{-2} vs. 15.8 mAh cm^{-2}, respectively, and showing smaller overpotential. Such behavior is imputed to fuller electrolyte impregnation resulting in better active material utilization in the case of the 44% porous electrode thereby improving its performance.

Regarding the influence of the pore size, the improved electrochemical performance in the case of 12 μm (16 μm) pore-sized electrodes could be attributed to the more isotropic pore morphologies (homogeneous tortuosities) in all three spatial directions when compared to 20 μm pore-sized electrodes according to the tomography analysis. Lower tortuosity values indicate shorter Li-ion migration paths thus ensuring faster Li-ion diffusivity. However, a big discrepancy was observed in the characteristic tortuosity values obtained by the tomography analysis and the EIS measurements (12 μm (16 μm): 1.52 μ-CT vs. 3.8 EIS; 20 μm: 1.76 μ-CT vs. 4.6 EIS) due to the inaccuracy of these methods, therefore making it hard to conclude which method is more precise and provides more accurate quantitative value. However, all these methods present the same trend and therefore could be used to qualitatively analyze and compare samples with different porosities and/or pore sizes.

Further investigation of thick binder-free electrodes could be performed, such as deeper investigation of the correlation between the pore anisotropy and the electrochemical performance and physical behavior during/after cycling. Obtained full pellets could be cycled in a full cell mode versus graphite to achieve comparable results to the commercially available batteries.

Acknowledgments

Authors would like to express gratitude to the Ministry of Higher Education & Research of France for the financial support of Dr. R. Elango via a “Contrat Doctoral” at UPJV Amiens, France as well as the LABEX-STOREX within the french Research Network on Electrochemical Energy Storage (RS2E), and National Centre for Scientific Research (CNRS) for the financial support of A. Nadeina.

References

[1] J.E. Harlow, X. Ma, J. Li, E. Logan, Y. Liu, N. Zhang, L. Ma, S.L. Glazier, M.M.E. Cormier, M. Genovese, S. Buteau, A. Cameron, J.E. Stark, J.R. Dahn, A Wide Range of Testing Results on an Excellent Lithium-Ion Cell Chemistry to be used as Benchmarks for New Battery Technologies, J. Electrochem. Soc. 166 (2019) A3031–A3044. doi:10.1149/2.0981913jes.

[2] S. Goutam, J. Timmermans, N. Omar, P. Van Den Bossche, J. Van Mierlo, Comparative Study of Surface Temperature Behavior of Commercial Li-Ion Pouch Cells of Different Chemistries and Capacities by Infrared Thermography, (2015) 8175–8192. doi:10.3390/en8088175.

[3] M. Abdel, K. Trad, N. Omar, O. Hegazy, B. Mantels, G. Mulder, P. Van Den Bossche, J. Van Mierlo, Lithium-ion batteries : Evaluation study of different charging methodologies based on aging process q, Appl. Energy. 152 (2015) 143–155. doi:10.1016/j.apenergy.2015.02.064.

[4] H. Lundgren, Electrochemical Characterization and Temperature Dependency of Mass-Transport Properties of LiPF 6 in EC : DEC, 162 (2015) 3–10. doi:10.1149/2.0641503jes.

[5] T. Aoshima, K. Okahara, C. Kiyohara, K. Shizuka, Mechanisms of manganese spinels dissolution and capacity fade at high temperature, 98 (2001) 378–381.

[6] F. Mestre-aizpurua, S. Hamelet, C. Masquelier, M.R. Palacín, High temperature electrochemical performance of nanosized LiFePO 4, 195 (2010) 6897–6901. doi:10.1016/j.jpowsour.2010.03.097.

[7] B. Kang, G. Ceder, Battery materials for ultrafast charging and discharging., Nature. 458 (2009) 190–193. doi:10.1038/nature07853.

[8] N. Ding, W. Chien, T.S.A. Hor, R. Lum, In fl uence of carbon pore size on the discharge capacity of Li – O 2 batteries †, (2014) 12433–12441. doi:10.1039/c4ta01745e.

[9] J. Chmiola, G. Yushin, R. Dash, Y. Gogotsi, Effect of pore size and surface area of carbide derived carbons on specific capacitance, 158 (2006) 765–772. doi:10.1016/j.jpowsour.2005.09.008.

[10] E. Environ, S. Kondrat, C.R. P, Environmental Science Effect of pore size and its dispersity on

the energy storage in nanoporous supercapacitors, (2012) 6474–6479. doi:10.1039/c2ee03092f.

[11] A. V Virkar, J. Chen, C.W. Tanner, J. Kim, The role of electrode microstructure on activation and concentration polarizations in solid oxide fuel cells q, 131 (2000) 189–198.

[12] K.. Huang, J.B. Goodenough, Solid Oxide Fuel Cell Technology, 1st ed., Woodhead Publishing, 2009.

[13] J.S. Wang, P. Liu, E. Sherman, M. Verbrugge, H. Tataria, Formulation and characterization of ultra-thick electrodes for high energy lithium-ion batteries employing tailored metal foams, J. Power Sources. 196 (2011) 8714–8718. doi:10.1016/j.jpowsour.2011.06.071.

[14] T. Takeuchi, M. Tabuchi, A. Nakashima, T. Nakamura, Y. Miwa, H. Kageyama, K. Tatsumi, Preparation of dense LiFePO4/C composite positive electrodes using spark-plasma-sintering process, in: J. Power Sources, 2005. doi:10.1016/j.jpowsour.2005.03.099.

[15] A. Vu, Y. Qian, A. Stein, Porous Electrode Materials for Lithium-Ion Batteries – How to Prepare Them and What Makes Them Special, (2012). doi:10.1002/aenm.201200320.

[16] H. Zheng, L. Tan, G. Liu, X. Song, V.S. Battaglia, Calendering effects on the physical and electrochemical properties of Li[Ni 1/3Mn 1/3Co 1/3]O 2 cathode, J. Power Sources. 208 (2012) 52–57. doi:10.1016/j.jpowsour.2012.02.001.

[17] W. Lai, C.K. Erdonmez, T.F. Marinis, C.K. Bjune, N.J. Dudney, F. Xu, R. Wartena, Y.M. Chiang, Ultrahigh-energy-density microbatteries enabled by new electrode architecture and micropackaging design, Adv. Mater. 22 (2010) 139–144. doi:10.1002/adma.200903650.

[18] J.S. Sander, R.M. Erb, L. Li, A. Gurijala, Y.M. Chiang, High-performance battery electrodes via magnetic templating, Nat. Energy. 1 (2016) 1–7. doi:10.1038/nenergy.2016.99.

[19] R. Amin, B. Delattre, A.P. Tomsia, Y.M. Chiang, Electrochemical Characterization of High Energy Density Graphite Electrodes Made by Freeze-Casting, ACS Appl. Energy Mater. 1 (2018) 4976–4981. doi:10.1021/acsaem.8b00962.

[20] J. Landesfeind, J. Hattendorff, A. Ehrl, W.A. Wall, H.A. Gasteiger, Tortuosity Determination of Battery Electrodes and Separators by Impedance Spectroscopy, J. Electrochem. Soc. 163 (2016)

A1373–A1387. doi:10.1149/2.1141607jes.

[21] S. Malifarge, B. Delobel, C. Delacourt, Determination of Tortuosity Using Impedance Spectra Analysis of Symmetric Cell, J. Electrochem. Soc. 164 (2017) E3329–E3334. doi:10.1149/2.0331711jes.

[22] M. Ebner, D.W. Chung, R.E. García, V. Wood, Tortuosity anisotropy in lithium-ion battery electrodes, Adv. Energy Mater. 4 (2014) 1–6. doi:10.1002/aenm.201301278.

[23] A.C. Forse, J.M. Griffin, C. Merlet, J. Carretero-Gonzalez, A.R.O. Raji, N.M. Trease, C.P. Grey, Direct observation of ion dynamics in supercapacitor electrodes using in situ diffusion NMR spectroscopy, Nat. Energy. 2 (2017). doi:10.1038/nenergy.2016.216.

[24] L. Hu, F. La Mantia, H. Wu, X. Xie, J. McDonough, M. Pasta, Y. Cui, Lithium-ion textile batteries with large areal mass loading, Adv. Energy Mater. 1 (2011) 1012–1017. doi:10.1002/aenm.201100261.

[25] F. Lalère, J.B. Leriche, M. Courty, S. Boulineau, V. Viallet, C. Masquelier, V. Seznec, An all-solid state NASICON sodium battery operating at 200??C, J. Power Sources. 247 (2014) 975–980. doi:10.1016/j.jpowsour.2013.09.051.

[26] A. Aboulaich, R. Bouchet, G. Delaizir, V. Seznec, L. Tortet, M. Morcrette, P. Rozier, J.M. Tarascon, V. Viallet, M. Dollé, A new approach to develop safe all-inorganic monolithic li-ion batteries, Adv. Energy Mater. 1 (2011) 179–183. doi:10.1002/aenm.201000050.

[27] R. Elango, A. Demortière, V. De Andrade, M. Morcrette, V. Seznec, Thick Binder-Free Electrodes for Li–Ion Battery Fabricated Using Templating Approach and Spark Plasma Sintering Reveals High Areal Capacity, Adv. Energy Mater. 8 (2018) 1–8. doi:10.1002/aenm.201703031.

[28] H. Zheng, J. Li, X. Song, G. Liu, V.S. Battaglia, A comprehensive understanding of electrode thickness effects on the electrochemical performances of Li-ion battery cathodes, Electrochim. Acta. 71 (2012) 258–265. doi:10.1016/j.electacta.2012.03.161.

[29] S. Range, M. Epple, Nanoscopic NaCl crystals as water-soluble porogens for polymer

membranes, RSC Adv. 2 (2012) 6650. doi:10.1039/c2ra01237e.

[30] Fiji: ImageJ, with “Batteries Included",(n.d.)., (n.d.). https://fiji.sc/.

[31] G. Siraudin, SOLUTION - Amira for Life Sciences, (2018). https://www.fei.com/software/amira/.

[32] C. Ahrens, James, Geveci, Berk, Law, ParaView: An End-User Tool for Large Data Visualization, in: Vis. Handb., Elsevier, 2005.

[33] K. Sun, T.S. Wei, B.Y. Ahn, J.Y. Seo, S.J. Dillon, J.A. Lewis, 3D printing of interdigitated Li-ion microbattery architectures, Adv. Mater. 25 (2013) 4539–4543. doi:10.1002/adma.201301036.

[34] C. Bae, C.K. Erdonmez, J.W. Halloran, Y. Chiang, Design of Battery Electrodes with Dual-Scale Porosity to Minimize Tortuosity and Maximize Performance, (2013) 1254–1258. doi:10.1002/adma.201204055.

[35] S.J. Cooper, A. Bertei, P.R. Shearing, J.A. Kilner, N.P. Brandon, TauFactor: An open-source application for calculating tortuosity factors from tomographic data, SoftwareX. 5 (2016) 203–210. doi:10.1016/j.softx.2016.09.002.

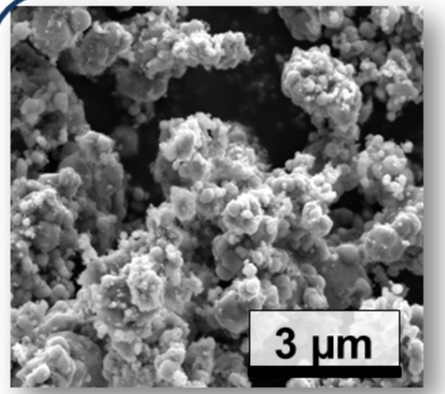

$LiFePO_4$

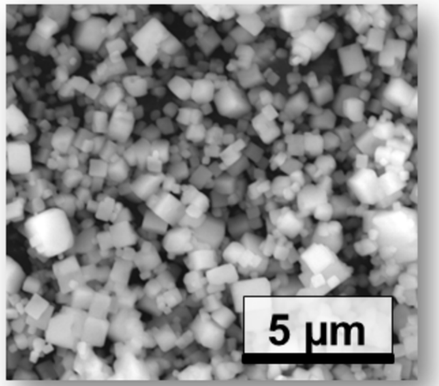

NaCl

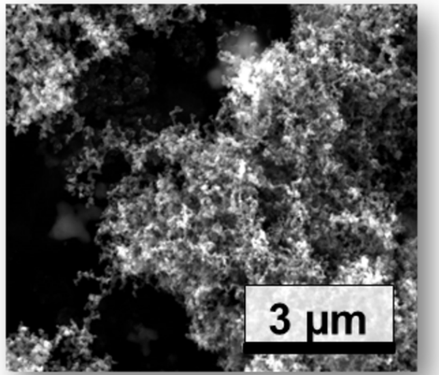

sp-Carbon

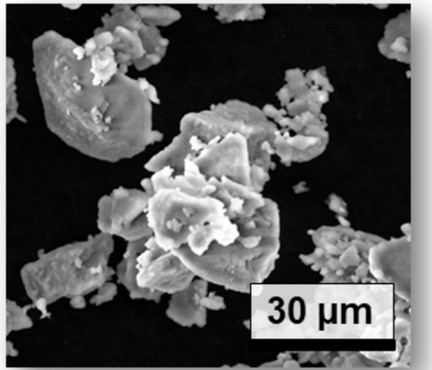

Mixing

Sintering

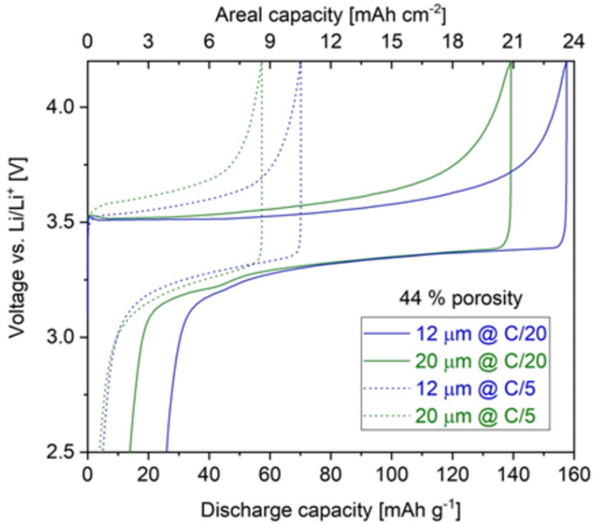

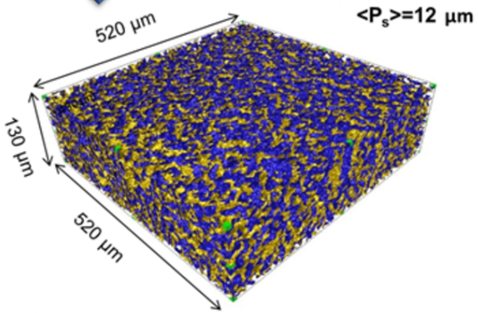

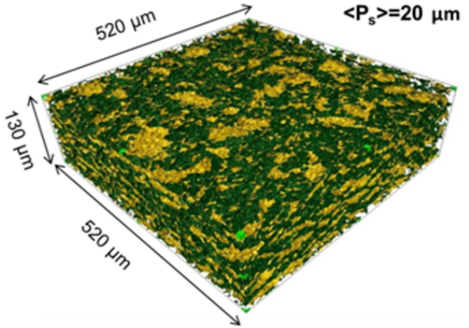

Electrode's architecture and electrochemistry correlation study